metals

MDPI

Article

Investigation of the Y Effect on the Microstructure Response and Radiation Hardening of PM V-4Cr-4Ti Alloys after Irradiation with D Ions

Yifan Zhang [1,2,3], Xiaoyuan Sun [1], Bing Ma [1,3], Jing Wang [1,*], Laima Luo [1] and Yucheng Wu [1]

[1] School of Materials Science and Engineering, Hefei University of Technology, Hefei 230009, China
[2] School of Material Science and Engineering, University of Science and Technology Beijing, Beijing 100083, China
[3] Engineering Research Center of High-Performance Copper Alloy Materials and Processing, Ministry of Education, Hefei 230009, China
* Correspondence: jwang@hfut.edu.cn

Abstract: In the current work, an analysis of the effects of Y on the radiation hardening and microstructure response of a V-4Cr-4Ti alloy has been conducted after 30 keV D ion irradiation at room temperature using transmission electron microscopy (TEM) and nanoindentation. The results show that the formation of large Y_2O_3 and small $Y_2V_2O_7$ nanoparticles was confirmed, indicating that the addition of Y reduces the amount of dissolved oxygen. The addition of Y has been shown to affect the radiation-induced dislocation loops, radiation hardening, and Ti-rich segregation of the V-4Cr-4Ti alloy. With the addition of Y, the mean size of the radiation-induced dislocation loop decreased, which may result from the strong sink strength of the nanoparticle/matrix interface, interactions between Y atoms and SIA clusters, and the strong binding energy of vacancy–oxygen pairs. Some particles with core–shell structures were observed after ion irradiation, where Ti-rich segregations at the nanoparticle/matrix interface were confirmed. These results indicate that Y might promote abnormal segregation. Possible causes for this include the lower interface energy at the particle/matrix interface and the interaction between oxygen and solute atoms.

Keywords: ion irradiation; vanadium alloy; powder metallurgy; yttrium; segregation

Citation: Zhang, Y.; Sun, X.; Ma, B.; Wang, J.; Luo, L.; Wu, Y. Investigation of the Y Effect on the Microstructure Response and Radiation Hardening of PM V-4Cr-4Ti Alloys after Irradiation with D Ions. *Metals* **2023**, *13*, 541. https://doi.org/10.3390/met13030541

Academic Editor: Ilana Perelshtein

Received: 8 February 2023
Revised: 28 February 2023
Accepted: 6 March 2023
Published: 8 March 2023

1. Introduction

Deuterium-tritium fusion is an option for a future source of nearly limitless and clean energy. Up to now, several candidate structural materials were proposed, including Reduced Activation Ferritic/Martensitic (RAFM) steels, oxide-dispersion-strengthened (ODS) steels, vanadium alloys, and SiCf/SiC composite. Vanadium alloys exhibit good chemical compatibility with liquid lithium, good mechanical properties at high temperatures, enhanced irradiation swelling resistance, and low activation [1–3]. Therefore, vanadium alloys have been considered a promising candidate structural material for future fusion reactors. Among the typical vanadium-based alloys, V–4Cr–4Ti [4] alloy is noteworthy, where a Cr element is added to enhance high temperature strength and creep resistance, and a Ti element is added to improve the resistance to irradiation-induced void swelling [5]. However, the high sensitivity of interstitial impurities (such as oxygen, carbon, and nitrogen) limited the application and fabrication of vanadium alloys. Previous studies have reported that high-level impurities promote the formation of Ti(CNO) precipitates, causing abnormal hardening and embrittlement increase [6–9]. Furthermore, first-principles calculations by Zhang showed that dissolved impurities (such as C, N, and O) could improve the generalized stacking-fault energy of (112)<111> and (110)<111> slip systems in bcc V matrix resulting in a strong hardening [10,11]. Thus, the content of impurities in raw materials and the preparation process must be controlled.

In recent years, the addition of Y in V-4Cr-4Ti alloys has been proposed as a means of improving its resistance to impurities, enhancing its mechanical performance [12,13], and suppressing irradiation evolution [14–16]. Luo et al. reported that the addition of 1 wt.% Y into a V-4Cr-4Ti alloy suppresses the formation of Ti-rich precipitates leading to improved mechanical performance [12]. Our previous study also demonstrated that the addition of Y to a V-4Cr-4Ti alloy improves plasticity, with the elongation of a Y-doped V-4Cr-4Ti alloy being almost double that of a V-4Cr-4Ti alloy [13]. Research by Watanabe et al. showed that the addition of Y can suppress microstructural evolution during ion and neutron irradiation [14–16]. Our previous study also demonstrated better irradiation resistance of a Y-doped V-4Cr-4Ti alloy at high temperature (450 °C) He ion irradiation [13]. Due to the limitation of solid solubility, powder metallurgy (PM) is typically used to prepare high-content V-Y alloys, which makes it possible to prepare dispersion-strengthened V-based alloys. As reported, V-4Cr-4Ti strengthened with Y-rich or Ti-rich nanoparticles exhibits good mechanical properties, lower irradiation hardening [17,18], and different evaluation of Ti (CNO) precipitates [19,20]. Deng and Duan reported that PM V-4Cr-4Ti-1.5Y-xTi_3SiC_2 alloy, which was strengthened by various kinds of Y-rich and Ti-rich nanoparticles, has higher mechanical properties and lower irradiation hardening rate compared with PM V-4Cr-4Ti alloy [17,18]. This kind of dispersion-strengthened V alloy exhibits a very different trend in the evaluation of Ti (CNO) precipitates after irradiation, which affect its irradiation resistance [19,20]. In our previous research, we observed abnormal hardening of a V-4Cr-4Ti-2Y alloy induced by input oxygen and oxygen segregation after irradiation with He ions at 450 °C [13]. However, the nanohardness was measured using the continuous stiffness method (CSM), of which the measurement stage takes a long time. This may lead to confusion regarding whether the surface oxidation is caused by irradiation, sample preparation, cooling stages after high temperature irradiation, or nanoindentation measurement.

This study investigated the microstructure and hardness of PM V-4Cr-4Ti and V-4Cr-4Ti-2Y alloys before and after 30 keV D ion irradiation. Radiation-induced dislocation loops, radiation hardening, and Ti-rich segregation with and without Y addition were examined using TEM, STEM, EDS, and nanoindentation. To avoid the surface oxidation caused by the long measurement and cooling stages, room temperature irradiation and a rapid hardness test based on the displacement–load relationship were used. We hope that these works will help in understanding the irradiation damage, irradiation hardening, and the effect of impurity atoms in vanadium alloys

2. Experimental

The V-4Cr-4Ti and V-4Cr-4Ti-2Y alloys utilized in this study were prepared via mechanical alloying (MA) and spark plasma sintering (SPS). The MA process was carried out with a milling time of 40 h and a milling speed of 270 rpm. The SPS process was carried out with a pressure of 40 MPa at 1423 K for 5 min. The chemical compositions of both alloys were determined using X-ray Fluorescence Spectrometer (XRF) analysis and are presented in Table 1. The samples for TEM observation were prepared using a Struers TenuPol-51 automatic twin-jet electro polisher with an electrolytic solution of sulfuric acid and methanol with a rate of 1:6. Samples for nanohardness test were mechanically sanded with 10,000-grit diamond sandpaper and then electrolytic-polished using the same parameters on the twin-jet electro polisher. A detailed experimental procedure for material preparation was described in our previous publication [13].

Table 1. Chemical composition of two kinds of V alloy (wt.%).

Materials	Cr	Ti	Zr	C	N	O	Y	V
V-4Cr-4Ti	4.62	4.22	0.08	0.02	0.04	0.21	-	Bal.
V-4Cr-4Ti-2Y	4.38	4.06	0.03	0.02	0.04	0.24	1.86	Bal.

All samples (both TEM sample and nanohardness sample) were irradiated with 30 keV D ions to a fluence of 1×10^{17} ions/cm^2 at near room temperature. The background pressure was $<1 \times 10^{-3}$ Pa. The total irradiation time was about 1 h. The damage profile was estimated using SRIM software, where the "Quick Kinchin-Pease" mode was selected based on the recommendation of Stoller [21] and the displacement threshold energies for V, Cr, and Ti were set as 40 eV, 40 eV, and 30 eV [22], respectively. The density used in SRIM calculation was 5.94 g/cm^3 which was automatically calculated by SRIM software using an atomic ratio of V:Cr:Ti = 91.84:3.91:4.24. The damage profile and the concentration of D ions are shown in Figure 1, the damage peak was about 0.5 dpa at 220 nm and the peak concentration was 7.3 at.% at 290 nm. The dose rate was about 1.4×10^{-4} dpa/s. At the TEM observation area (approximately 100 nm in depth), the displacement damage was about 0.3 dpa and the D concentration was nearly 0.8 at.%. The inclusion of the temperature records from the two thermocouples during irradiation in Figure 1b is helpful in addressing the concerns about beam heating. In this work, standard TEM samples or nanoindentation samples were placed in a copper holder. The cooling system and main thermocouple were on the bottom of platform. A closer internal thermocouple was installed at the top of platform. During ion irradiation, the temperature was controlled near room temperature according to the value of the main thermocouple. The data showing that the temperature increase during irradiation was lower than 10 °C are reassuring.

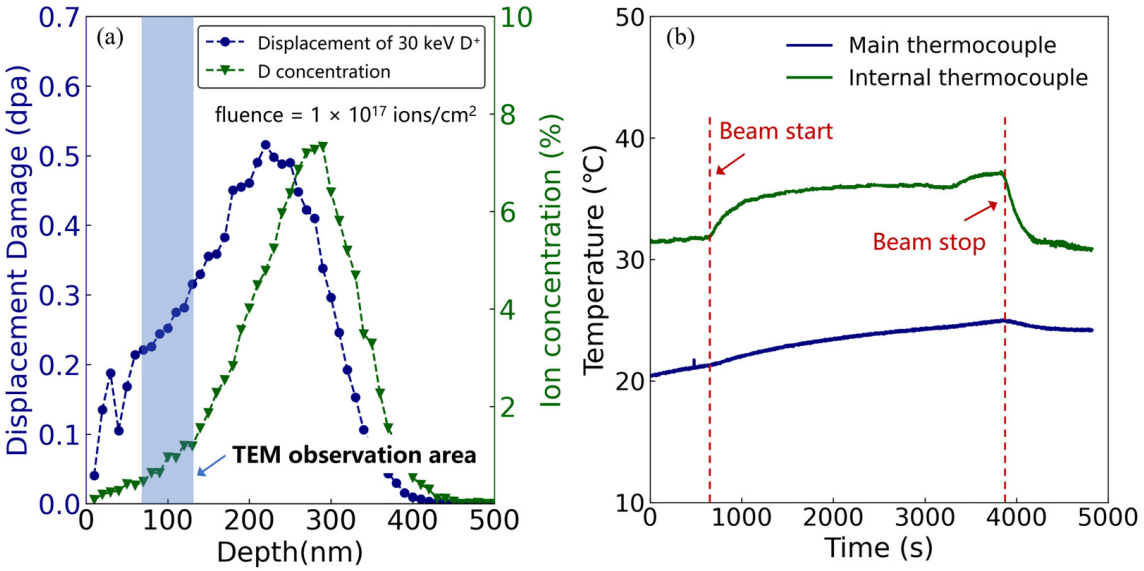

Figure 1. (**a**) The damage profiles of displacement damage and implanted D ions in V-4Cr-4Ti alloy calculated by using the software SRIM 2013 with the "Quick Kinchin-Pease" mode. (**b**) The temperature record measured by main and internal thermocouples during irradiation.

TEM and STEM observations were carried out using a FEI Tecnai G2 F20 TEM operated at 200 kV and the local thickness of TEM sample was estimated using the number of thickness fringes. The hardness was measured using a DUH-50 depth-sensing ultra-low-load indentation hardness tester with a Berkovich-type (trigonal pyramid) diamond tip. The maximum load was set as 0.01N, the loading rate was 0.001 N/s and the holding time was 1 s. The total hardness test time for a single position was about 11s.

3. Results and Discussion

3.1. Microstructure Analysis

The microstructure of V-4Cr-4Ti and V-4Cr-4Ti-2Y alloys was characterized using TEM. The TEM morphology of the V-4Cr-4Ti alloy is illustrated in Figure 2a, the results indicated that the V-4Cr-4Ti alloy has a grain size of 1–3 μm and no needle-shaped Ti(CNO)

precipitates appeared. This phenomenon may be due to the relatively low preparation temperature during PM fabrication. A STEM high-angle annular dark field (HAADF) image of nanoparticles in V-4Cr-4Ti-2Y alloys and corresponding HRTEM images are shown in Figure 2b–e. The chemical composition of nanoparticles was measured using EDS analysis and the result is shown in Figure 2f. As shown from images, two kinds of particles, the large and the small, were observed. Particle A was selected as an example of large Y-rich particles, which were also O-rich as shown in EDS results, and was identified as Y_2O_3. Particle B was selected as an example of a small particle and was identified as $Y_2V_2O_7$. The formation of these Y-O particles means that the oxygen was enriched, which can reduce the content of dissolved O in the V matrix and help to improve mechanical properties. This result suggests that the addition of Y contributes to reducing the dissolved oxygen and the product is Y-rich oxide nanoparticles.

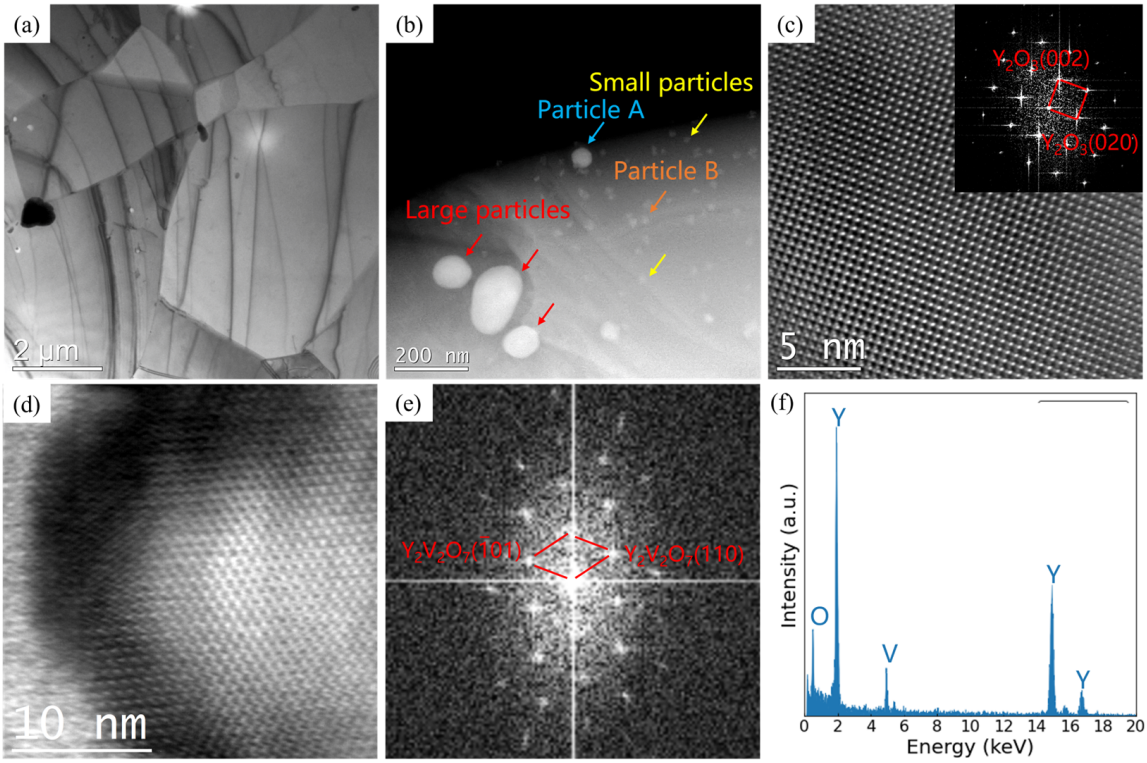

Figure 2. TEM images and corresponding EDS analysis of V-based alloys: (**a**) TEM image of V-4Cr-4Ti alloy; (**b**) STEM image of V-4Cr-4Ti-2Y alloy; (**c**) HRTEM image of Particle A (an example of large particle) and corresponding FFT image; (**d**) HRTEM image of Particle B (an example of small particle); (**e**) FFT image of (**d**); (**f**) EDS result of Particle A.

Figure 3 shows the X-ray diffraction (XRD) patterns of V-4Cr-4Ti and V-4Cr-4Ti-2Y alloys. The lattice parameters of the alloys were determined to be 0.30343 nm and 0.30288 nm, respectively. Stringer's previous work has reported that the lattice of bcc V increases with the addition of solid dissolved oxygen, and this increase shows a linear relationship with the content of dissolved oxygen [23]. Thus, the slight decrease in the lattice parameters of V-4Cr-4Ti-2Y suggests a reduction in the dissolved oxygen content. This finding is consistent with the TEM analysis.

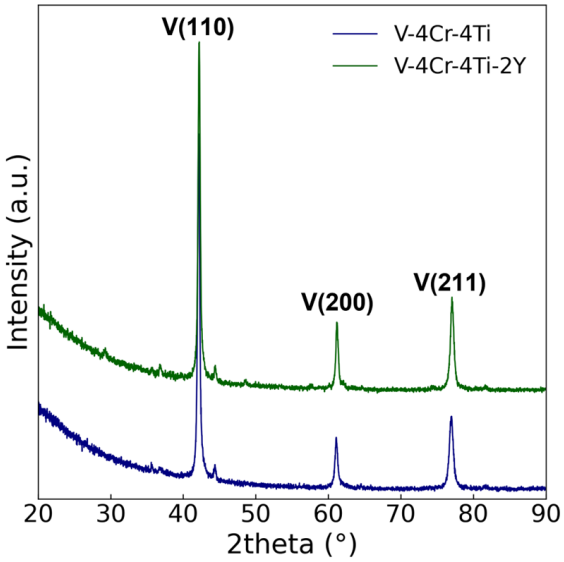

Figure 3. XRD patterns of V-4Cr-4Ti and V-4Cr-4Ti-2Y alloys.

3.2. Radiation-Induced Dislocation Loop

After ion irradiation, the radiation-induced dislocation loops in both alloys were characterized using TEM. The results are illustrated in Figure 4 and summarized in Figure 5. All images were taken in the same g vector (in this work, g vector was selected as $\boldsymbol{g} = (011)_V$), to obtain a similar dislocation contrast and diffraction extinction. Moreover, to avoid the effect of grain boundary on defect distribution, the observation area was selected far away from the grain boundary (the distance from the nearest grain boundary was no less than 50 nm) [24,25]. The size distribution of dislocation loops was statistically analyzed using the stereological method based on the analysis of TEM images with imageJ software, and the number density and mean dislocation loop size are summarized in Table 2. The mean dislocation loop size in the V-4Cr-4Ti alloy is 4.2 $\pm$ 1.4 nm, which is a little bit larger than that in the V-4Cr-4Ti-2Y alloy (3.7 $\pm$ 1.1 nm). In this paper, we utilized the standard deviation as the error bar to represent the statistics of the dislocation loop size distribution. Although the standard deviation and the mean can jointly determine the Gaussian distribution in mathematics, this does not imply that there is no significant difference with other means within the error bar. Therefore, to address this issue, we employed a two-sample t-test to test the significance of the dislocation ring size distribution in V-4Cr-4Ti and V-4Cr-4Ti-2Y alloys. As shown in Table 3, the results demonstrate that at a significance level of $\alpha = 0.05$ there is indeed a significant difference between the two distributions. This statistical difference in dislocation ring size supports the conclusion that the dislocation ring in the V-4Cr-4Ti-2Y alloy is relatively smaller. This difference also indicated that the V-4Cr-4Ti-2Y alloy has a higher radiation resistance compared with the V-4Cr-4Ti alloy. The number density was measured as about 5.5 $\times$ 10^{22} m^{-3} and 4.3 $\times$ 10^{22} m^{-3} in the V-4Cr-4Ti and V-4Cr-4Ti-2Y alloys, respectively. Due to the limitation of TEM statistics, it can be considered that the number density of dislocation loops in two kinds of alloy are at the same level.

It should be noted that the minimum size of the dislocation loops detected using Image J software was approximately 1.7 nm in diameter in the V-4Cr-4Ti-2Y alloy, which corresponded to approximately 15 pixels in a 2048 $\times$ 2048 TEM image. In contrast, the minimum size of the loops detected in the image of the V-4Cr-4Ti alloy was approximately 2.0 nm. When we set a threshold of 2 nm in the results of the V-4Cr-4Ti-2Y alloy, the mean size of the dislocation loops increased by only 0.05 nm, resulting in a rounded mean loop size of 3.8 nm, and the loop density decreased by approximately 2%. Despite this, the significant difference in the size of the dislocation loops between the two alloys could still be confirmed by a two-sample t-test at a significance level of $\alpha = 0.05$, as shown in Table 4.

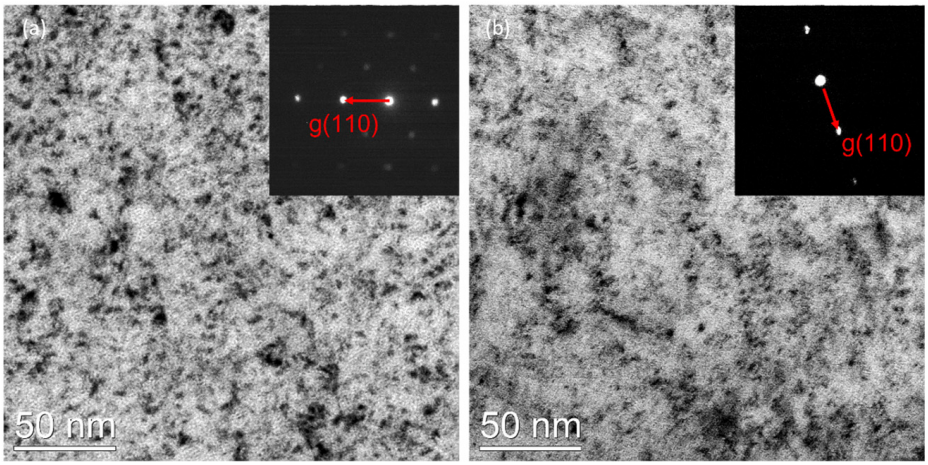

Figure 4. TEM images of radiation-induced dislocation loops in (**a**) V-4Cr-4Ti and (**b**) V-4Cr-4Ti-2Y.

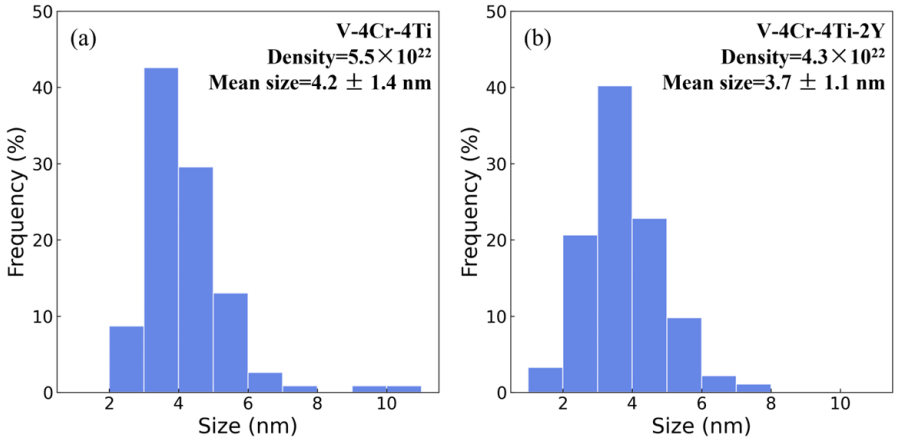

Figure 5. Size distribution of irradiation-induced dislocation loops in (**a**) V-4Cr-4Ti alloy and (**b**) V-4Cr-4Ti-2Y alloy.

Table 2. Number density and mean size of dislocation loops in V-4Cr-4Ti and V-4Cr-4Ti-2Y alloys.

Materials	Population	Number Density ρ (m^{-3})	Mean Size D (nm)
V-4Cr-4Ti	115	5.5×10^{22}	4.2 ± 1.4
V-4Cr-4Ti-2Y	92	4.3×10^{22}	3.7 ± 1.1

Table 3. The paired-sample *t*-test of the dislocation loop size distribution in both alloys.

	t Statistic	DF	Prob > |t|
Equal Variance Assumed	−3.11	205	0.0022
Equal Variance NOT Assumed (Welch Correction)	−3.18	204.99	0.0017

The smaller dislocation loops in the V-4Cr-4Ti-2Y alloy can be explained by the following mechanisms: Firstly, the strong sink strength of the nanoparticle/matrix interface promotes the absorption of interstitial atoms and vacancies, resulting in the reduction in radiation-induced dislocation loops [26]. This mechanism has been reported in various alloys [12,17,27]. Secondly, the interactions between Y atoms and self-interstitial atom (SIA) clusters hinder the aggregation of SIAs into large SIA loops, ultimately resulting in smaller mean loop size. Zhang and his colleagues reported that the maximum binding energy between Y atoms and SIA clusters in the V matrix is about 0.35 eV, which is much higher

than the maximum binding energy between Ti atoms and SIA clusters (about 0.07 eV) and the most common alloying elements in vanadium alloy (most are negative binding energies) [28]. However, it should be noted that the solubility of Y in the V matrix is quite low, which means that the solid-solution Y atoms are limited. Thus, the contribution of the nanoparticle/matrix interface should be dominant.

Table 4. The paired-sample *t*-test of the dislocation loop size distribution in both alloys with a threshold of 2 nm.

	t Statistic	DF	Prob > |t|
Equal Variance Assumed	2.84	203	0.0050
Equal Variance NOT Assumed (Welch Correction)	2.93	202.96	0.0038

Moreover, another mechanism may be the oxygen content. As reported by Deng et al. [29], the binding energy between a vacancy and an oxygen pair is stronger in the first nearest-neighbor distance (binding energy of 0.56 eV) than in other neighbor distances. This suggests that vacancies can serve as strong oxygen trappers in vanadium crystals. Surface oxidation leads to oxygen enrichment near the surface, which results in vacancies binding with oxygen atoms. Vacancy binding with oxygen atoms reduces the probability of recombination between vacancies and interstitial atoms, indicating that interstitial atoms are more likely to assemble to form interstitial dislocation loops, which are the main type of dislocation in room-temperature irradiation. The neutron irradiation of vanadium alloys at low temperatures in the Japan Material Testing Reactor also supports that interstitial oxygen promotes dislocation loop nucleation [30].

3.3. Radiation Hardening

The nanohardness of both V-4Cr-4Ti and V-4Cr-4Ti-2Y alloys before and after D ion irradiation was measured using a depth-sensing ultra-low-load indentation hardness tester. To minimize the effect of surface oxidation after irradiation, the hardness test was carried out immediately after ion irradiation. For non-irradiated samples, the test was conducted immediately after polishing. To reduce the time exposed to air, the hardness was obtained using the relationship between indenter displacement (d) and indenter load (L), which takes less test time compared with the CSM method. The maximum load was set at 1 gf, the loading rate was 0.1 gf/s, and the holding time was 1s. The total test time for a single position was 11 s. The test platform was kept at near room temperature during irradiation The hardness was calculated using Equation (1) [31,32]:

$$\frac{L}{d} = Ad + B \tag{1}$$

where A and B are parameters which are dependent on materials but independent of the load and the indenter displacement, and the value of A is proportional to the Vickers hardness (H_V) as shown in Equation (2):

$$A(GPa) = 0.287H_V \tag{2}$$

However, the low input ion damage resulted in a shallow damage layer. As a result, the hardness measurement of the irradiated samples is complex, including the indentation size effect (ISE), damage layer (displacement damage and gas concentration), and soft substrate effect (SSE). Although, according to Jiang [33], the effect of SSE is relatively low compared to that of the damage layer and ISE, it should be noted that it is unwise to completely ignore the effect of SSE in such shallow irradiation. The contribution of SSE to the hardness measurement deserves further experimental and numerical study. Therefore, the hardness was obtained by fitting the data between 100 and 200 nm to reduce the effects of ISE. This hardness measurement was used to analyze a very shallow damage layer

(about 100 nm in the SRIM calculation, caused by the irradiations of He and D ions at 10 keV) [32], and although the results will be affected by SSE, it is still meaningful for qualitative analysis.

Theoretically, the surface roughness also has a significant impact on the hardness measurement of nanoindentation. On the one hand, when the nanoindentation probe is pressed into the sample surface, the roughness will lead to the change of material displacement. On the other hand, the rougher surface will also lead to higher probe passivation rate. Both will increase the error of hardness measurement. Mechanistically, the generation of irradiation swelling (such as bubbles or voids) and the sputter deposition process are the main factors that may affect the surface roughness of irradiated samples. However, it is unlikely that either of these factors significantly impact surface roughness under the selected D ion irradiation parameters: Firstly, the irradiation was carried out at near room temperature, and the damage peak was less than 1 dpa. Observing irradiation swelling under such parameters is difficult, indicating that swelling is unlikely to affect the surface roughness after irradiation. For example, as reported in Jiang's work, no bubbles or voids were observed in the room-temperature irradiation of 80 keV He ions with a fluence of 1×10^{21} ions/cm^2 and an irradiation of 80 keV He ions (with a fluence of 1×10^{21} ions/cm^2) + 50 keV H ions (with a fluence of 1×10^{21} ions/cm^2). Secondly, the sputter deposition process commonly occurs during high-flux plasma exposure. However, the fluence of D ion irradiation (1×10^{17} ions/cm^2) is significantly lower than that of plasma exposure (usually 10^{23}~10^{24}/m^2), making any change in surface roughness caused by sputter deposition during irradiation negligible. Obvious evidence for this is that the thin area of the TEM sample did not fall off after irradiation, and the mass thickness contrast caused by the concave–convex was not observed. Thus, it can be inferred that the change of surface roughness was insignificant.

However, this does not necessarily rule out the possibility of measurement errors caused by random or accidental factors. To ensure accuracy and reliability, we conducted four separate measurements for each sample, and the resulting measurements for the load/displacement–displacement (*L/d-d*) plots of all samples are presented in Figure 6. As we can see, the *L/d-d* plots show a linear relationship generally. As shown in Figure 7 the averages hardness of the V-4Cr-4Ti alloy before and after irradiation was measured as 192 ± 25 HV and 237 ± 17 HV, respectively. The radiation hardening is ΔH = 45 ± 30 HV and the hardening rate is calculated to be approximately 23.4%. The hardness of the V-4Cr-4Ti-2Y alloy was measured as 110 ± 13 HV and 132 ± 13 HV before and after irradiation. The radiation hardening of V-4Cr-4Ti-2Y is (ΔH = 22 ± 18 HV), which is slightly lower, and the hardening rate is 20.1%.

Typically, the radiation hardening can be described by the dispersed barrier hardening (DBH) model, as Equation (3) [34,35]:

$$\Delta\sigma = M\alpha'\mu b\sqrt{ND} \tag{3}$$

where $\Delta\sigma$ is the strength and hardness increments after irradiation. M = 3.06 is the Taylor factor and α' = 0.3 is a constant for dislocation loops. μ = 47 GPa is the shear modulus of the vanadium matrix (pure vanadium), b is the burgers vector of dislocation. N and D are the number density and the mean size of dislocation loops. As described above, the smaller dislocation loops contribute to the lower radiation hardening in the V-4Cr-4Ti-2Y alloy.

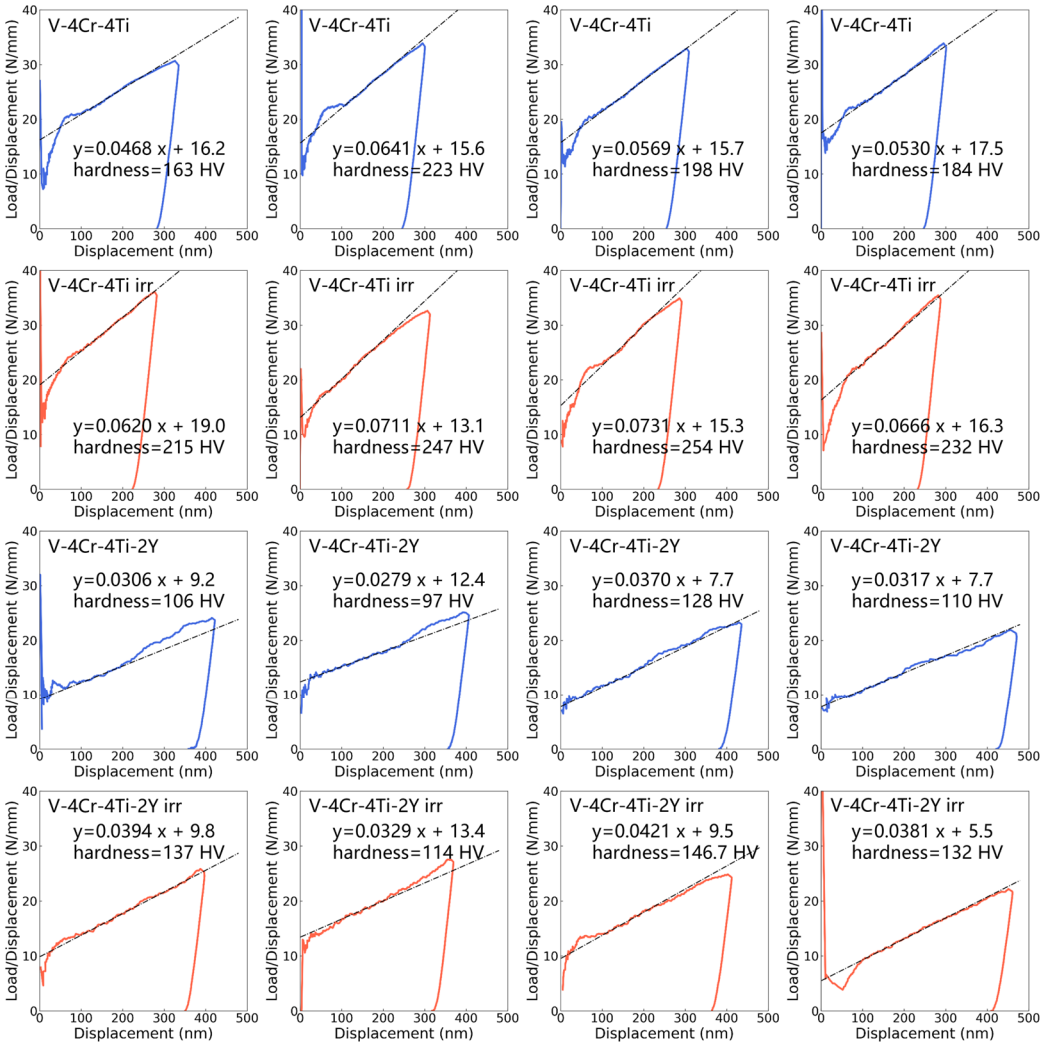

Figure 6. Typical *L*/*d*-*d* plots of all samples and fitting results using the least squares method are marked with black dotted line.

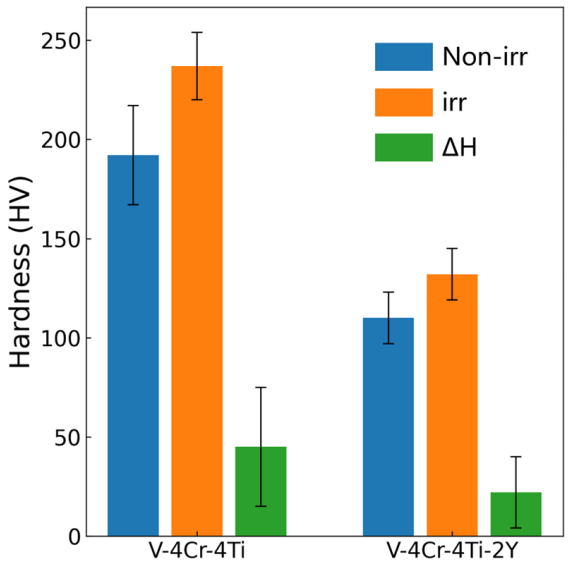

Figure 7. The average hardness of V-4Cr-4Ti and V-4Cr-4Ti-2Y alloys before and after D ion irradiation.

Interestingly, the gradient of the *L/d-d* plot increases at shallow subsurface regions in V-4Cr-4Ti and unirradiated V-4Cr-4Ti-2Y alloys. These sublayers were about 70 nm in depth in the V-4Cr-4Ti alloy (both before and after irradiation). However, it was almost zero in the unirradiated V-4Cr-4Ti-2Y alloy. In the irradiated V-4Cr-4Ti alloy, the sublayers were slightly deepened. This phenomenon may be due to complex surface effects, size effect, and surface oxidation. Since the depths of sublayers were almost zero, we suggest that the contribution of surface oxidation cannot be ignored. As a result of the high chemical activity of vanadium alloys, it is very difficult to prevent the oxygen absorption on the surface. This solid dissolved oxygen will cause the hardening of the V base alloy. As reported by Deng, the maximum binding energy between Ti atoms and O atoms in the V matrix is about 0.4 eV, which is lower than the maximum binding energy between Y atoms and O atoms (about 0.6 eV), but much higher than that of Cr-O (less than 0.1 eV) [29]. In all common alloy elements in V-based alloys, Y atoms have the greatest tendency to bind with oxygen followed by Ti atoms. Thus, the addition of Y can reduce the solid dissolved oxygen and weaken its influence on mechanical properties. Thus, we can see a shallower sublayer in V-4Cr-4Ti-2Y. Similarly, due to the surface oxidation during irradiation the sublayer was deeper in V-4Cr-4Ti-2Y.

3.4. Ti-Rich Segregation

To analyze the microstructure changes in the sublayer, STEM analysis was carried out at a very thin area (where the thickness is less than 50 nm), and the results are listed in Figure 8. Figure 8a shows the small nanoparticles distributed in the V matrix, and Figure 8b shows the EDS element distribution near two neighborly particles. As shown in Figure 8b, Ti-rich shells were obviously clearly observed at the nanoparticle/matrix interface, indicating Ti segregation towards the interface. In V-based alloys, Ti plays the role of purifying the matrix. This abnormal segregation may lead to the inhomogeneous distribution of Ti atoms and the additional uncertainty about the long-term service performance of V-based alloys. A reasonable explanation for the formation of these core–shell structures is that Ti segregation is related to radiation-induced segregation during D ion irradiation based on the following mechanisms:

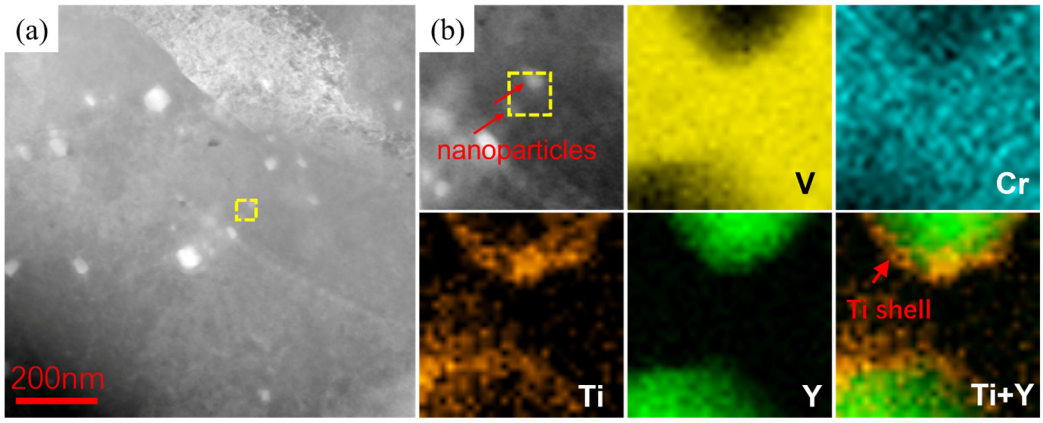

Figure 8. STEM images and corresponding EDS element distribution near nanoparticles in V-4Cr-4Ti-2Y alloy: (**a**) STEM image; (**b**) EDS element distribution of the yellow-boxed area.

Firstly, the Ti shell results from Ti segregation at the particle/matrix interface due to the lower interface energy at the particle/matrix interface. This mechanism is similar to the Cr shell in various irradiated ODS steels, such as the Cr-coated Ti-Y-O particle in PM2000 and 14Cr-ODS steel reported by Ribis and Jung [36,37]. Additionally, some other kinds of shells, such as Y, Si, Ni, and Mn, have also been reported in irradiated ODS steel [38–40]. These results demonstrate that the formation of irradiation-induced core–shell nanoparticles is possible.

Secondly, the interaction between oxygen and solute atoms may play a significant role. As described above, Y atoms have the greatest tendency to bind with oxygen followed by Ti atoms. Due to the input of oxygen from the environmental atmosphere, and the segregation of oxygen [13], the oxygen content of the sublayer increased during irradiation. Therefore, when most Y atoms near the surface were combined oxygen, Ti diffused toward Y-rich particles, leaving a Ti-coated Y-rich particle. This phenomenon also suggests that Y near the surface has been completely exhausted.

Thirdly, the motions of vacancy may be another reason. In the presented V-based alloy, the size of the Ti atom (about 140 pm) is larger than the V atom (about 135 pm) [41]. Vacancies are easier to exchange with the Ti atoms due to the bigger atom size. During irradiation, the concentration gradient of vacancies drives vacancies to flow from the matrix to the interface because of the high sink strength of the nanoparticle/matrix interface. The exchange could lead to a migration of Ti atoms in the same direction of vacancies, and finally leave a Ti enrichment in the particle/matrix interface.

4. Conclusions

An analysis of the effects of Y on the radiation hardening and microstructure response of a V-4Cr-4Ti alloy after 30 keV D ion irradiation has been conducted using TEM and nanoindentation. Based on the above results and analysis, the following conclusions can be drawn:

1. The formation of large Y_2O_3 and small $Y_2V_2O_7$ nanoparticles was confirmed, indicating that the addition of Y reduces the amount of dissolved oxygen, resulting in the formation of Y-rich oxide nanoparticles.
2. The addition of Y reduces the size of radiation-induced dislocation loops and slightly reduces radiation hardening after room temperature irradiation. Possible causes for this include the strong sink strength of the nanoparticle/matrix interface, interactions between Y atoms and SIA clusters, and the strong binding energy of vacancy–oxygen pairs.
3. Ti-rich shells coated with Y-rich particles were observed in the sublayer near the surface of the Y-doped V-4Cr-4Ti alloy after irradiation at room temperature, proving that the addition of Y in the V-4Cr-4Ti alloy affects Ti segregation. Possible causes for this include the lower interface energy at the particle/matrix interface and the interaction between oxygen and solute atoms.

In the future, we plan to further analyze the effects of Y on solid dissolved oxygen, irradiation defects, and Ti precipitation in vanadium alloys. This is especially important given that Ti is a key alloying element in vanadium alloys. The presence of a Ti shell on Y-rich particles may have an impact on the long-term service behavior of vanadium alloys.

Author Contributions: Writing—original draft preparation, Y.Z.; investigation, X.S. and B.M.; writing—review and editing, J.W.; project administration, L.L. and Y.W. All authors have read and agreed to the published version of the manuscript.

Funding: This work was supported by National MCF Energy R&D Program (2022YFE03140000, 2022YFE03210200), National Key Research and Development Program of China (2019YFE03120002), the National Science Foundation of China (12205070, 12205071), Natural Science Foundation of Anhui Province (2208085QA20), and the Fundamental Research Funds for the Central Universities (JZ2022HGQA0119 and PA2022GDGP0029).

Data Availability Statement: The data presented in this study are available on request from the corresponding author.

Acknowledgments: The authors are grateful to Qian Zhan for the helpful discussion and constructive comments on the manuscript.

Conflicts of Interest: The authors declare no conflict of interest.

References

1. Muroga, T.; Chen, J.M.; Chernov, V.M.; Kurtz, R.J.; Le, F.M. Present status of vanadium alloys for fusion applications. *J. Nucl. Mater.* **2014**, *455*, 263–268. [CrossRef]
2. Li, Z.D.; Li, Q.; Li, Y.; Ma, T.D. Microstructure and properties of V–5Cr–5Ti alloy after hot forging. *Fusion Eng. Des.* **2018**, *127*, 83–90. [CrossRef]
3. Pint, B.A.; Pawel, S.J.; Howell, M.; Moser, J.L.; Garner, G.W.; Santella, M.L.; Tortorelli, P.F.; Wiffen, F.W.; DiStefano, J.R. Initial characterization of V–4Cr–4Ti and MHD coatings exposed to flowing Li. *J. Nucl. Mater.* **2009**, *386*, 712–715. [CrossRef]
4. Chen, J.M.; Chernov, V.M.; Kurtz, R.J. Overview of the vanadium alloy researches for fusion reactors. *J. Nucl. Mater.* **2011**, *417*, 289–294. [CrossRef]
5. Muroga, T. Vanadium for Nuclear Systems. *Compr. Nucl. Mater.* **2012**, *4*, 391–406.
6. Duquesnes, V.; Guilbert, T.; Flem, M.L. French investigation of a new V–4Cr–4Ti grade: CEA-J57–Fabrication and microstructure. *J. Nucl. Mater.* **2012**, *426*, 96–101. [CrossRef]
7. Zhu, B.; Yang, S.; Ding, J.; Zhang, W.; Long, Y.; Wan, F. Abnormal hardening effect induced by the lath-like precipitates in the V-4Cr-4Ti alloy. *Mater. Lett.* **2015**, *161*, 609–612. [CrossRef]
8. Jiang, S.N.; Xu, L.Q.; Wan, F.R. Effect of precipitates on high-temperature strength and irradiation behavior of vanadium-based alloys. *J. Iron Steel Res. Int.* **2018**, *25*, 1270–1277. [CrossRef]
9. Muroga, T.; Nagasaka, T.; Watanabe, H.; Yamazaki, M. The effect of final heat treatment temperature on radiation response of V-4Cr-4Ti. *J. Nucl. Mater.* **2011**, *417*, 310–313. [CrossRef]
10. Zhang, X.M.; Li, Y.F.; Tang, J.F.; Deng, L.; Li, W.; Wang, L.; Deng, H.Q.; Hu, W.Y. Precipitate/vanadium interface and its strengthening on the vanadium alloys: A first-principles study. *J. Nucl. Mater.* **2019**, *527*, 151821. [CrossRef]
11. Zhang, X.; Tang, J.; Deng, L.; Zhong, G.; Liu, X.; Li, Y.; Deng, H.; Hu, W. The effects of interstitial impurities on the mechanical properties of vanadium alloys: A first-principles study. *J. Alloys Compd.* **2017**, *701*, 975–980. [CrossRef]
12. Luo, H.T.; Luo, F.F.; Chen, Y.H.; Wang, J.W.; Liu, Q.X.; Li, F.; Xie, Z.Y.; Lin, W.B.; Guo, L.P. Effect of yttrium content on microstructure and irradiation behavior of V-4Cr-4Ti-xY alloys. *J. Nucl. Mater.* **2022**, *559*, 153480. [CrossRef]
13. Zhang, Y.F.; Li, R.R.; Diao, S.Z.; Wan, F.R.; Zhan, Q. Plasticity Improvement and Radiation Hardening Reduction of Y Doped V-4Cr-4Ti Alloy. *J. Nucl. Mater.* **2022**, *560*, 153508. [CrossRef]
14. Watanabe, H.; Muroga, T.; Nagasak, T. Effects of Irradiation Environment on V–4Cr–4Ti Alloys. *Plasma Fusion Res.* **2017**, *12*, 2405011. [CrossRef]
15. Watanabe, H.; Higashijima, A.; Yoshida, N.; Nagasaka, T.; Muroga, T. The microstructure of laser welded Y doped V-4Cr-4Ti alloys after ion irradiation. *J. Nucl. Mater.* **2009**, *386*, 598–601. [CrossRef]
16. Watanabe, H.; Yamasaki, K.; Higashijima, A.; Taguma, H.; Nagasaka, T.; Muroga, T. Microstructural changes of Y-doped V-4Cr-4Ti alloys after ion and neutron irradiation. *Nucl. Mater. Energy* **2016**, *9*, 447–450. [CrossRef]
17. Zheng, P.F.; Chen, J.M.; Nagasaka, T.; Muroga, T.; Zhao, J.J.; Xu, Z.Y.; Li, C.H.; Fu, H.Y.; Chen, H.; Duan, X.R. Effects of dispersion particle agents on the hardening of V–4Cr–4Ti alloys. *J. Nucl. Mater.* **2014**, *455*, 669–675. [CrossRef]
18. Duan, X.R.; Chen, J.M.; Feng, K.M.; Liu, X.; Li, B.; Wu, J.H.; Wang, X.Y.; Zheng, P.F.; Wang, Y.Q.; Wang, P.H.; et al. Progress in fusion technology at SWIP. *Fusion Eng. Des.* **2016**, *109*, 1022–1027. [CrossRef]
19. Zhang, Y.F.; Du, J.K.; Liu, P.P.; Zheng, P.F.; Yang, S.W.; Wan, F.R.; Zhan, Q. Response of microstructure and hardening to deuterium ion irradiation inV-4Cr-4Ti-1.8Y-0.4Ti3SiC2 and V-4Cr-4Ti alloy. *Fusion Eng. Des.* **2020**, *159*, 111789. [CrossRef]
20. Krishnan, V.K.; Sinnaeruvadi, K.; Verma, S.K.; Dash, B.; Agrawal, P.; Subramanian, K. Yttria catalyzed microstructural modifications in oxide dispersion strengthened V–4Cr–4Ti alloys synthesized by field assisted sintering technique. *Philos. Mag.* **2017**, *97*, 1847–1865. [CrossRef]
21. Stoller, R.E.; Toloczko, M.B.; Was, G.S.; Certain, A.G.; Dwaraknath, S.; Garner, F.A. On the use of SRIM for computing radiation damage exposure. *Nucl. Instrum. Methods Phys. Res. Sect. B Beam Interact. Mater. At.* **2013**, *310*, 75–80. [CrossRef]
22. *NRT ASTM E521*; Standard Practice for Neutron Radiation Damage Simulation by Charged-Particle Irradiation. ASTM International, Annual Book of ASTM Standards; ASTM: Philadelphia, PA, USA, 1996.
23. Stringer, J. The vanadium-oxygen system—A review. *J. Less Common Met.* **1965**, *8*, 1–14. [CrossRef]
24. Zhang, L.; Du, Y.F.; Han, W.T.; Liu, P.P.; Yi, X.O.; Yabuuchi, K.; Ohnuki, S.; Wan, F.R. An approximate in-situ method for investigating irradiation damage of grain boundary. *Nucl. Mater. Energy* **2021**, *29*, 101056. [CrossRef]
25. Diao, S.Z.; Zhao, Q.; Wang, S.L.; Han, W.T.; Wang, Z.Q.; Liu, P.P.; Chen, Y.H.; Wan, F.R.; Zhan, Q. The microstructure evolution and irradiation hardening in 15Cr-ODS steel irradiated by helium ions. *Mater. Charact.* **2022**, *184*, 111699. [CrossRef]
26. Zhang, Y.F.; Zhan, Q.; Ohnuki, S.; Kimura, A.; Wan, F.R.; Yoshida, K.; Nagai, Y. Radiation-hardening and nano-cluster formation in neutron-irradiated 9Cr2W low activation steels with different Si contents. *J. Nucl. Mater.* **2019**, *517*, 1–8. [CrossRef]
27. Was, G.S. *Fundamentals of Radiation Materials Science: Metals and Alloys*; Springer: Berlin/Heidelberg, Germany, 2016.
28. Yu, H.Q.; Wang, S.L.; Zhang, Y.F.; Liu, Q.; Diao, S.Z.; Liu, P.P.; Oono, N.H.; Ukai, S.; Wan, F.R.; Ohnuki, S.; et al. Response of nanoclusters to heavy-ion irradiation in an Fe-12Cr ODS steel. *Fusion Eng. Des.* **2021**, *172*, 112759. [CrossRef]
29. Deng, L.; Tang, L.Z.; Zhang, X.M.; Tang, J.F.; Li, R.L.; Deng, H.Q. Ab initio solute–interstitial impurity interactions in vanadium alloys: The roles of vacancy. *RSC Adv.* **2016**, *6*, 78621–78628. [CrossRef]
30. Candra, L.; Fukumoto, K.; Kimura, A.; Matsui, H. Microstructural evolution and hardening of neutron irradiated vanadium alloys at low temperatures in Japan Material Testing Reactor. *J. Nucl. Mater.* **1999**, *271*, 301–305. [CrossRef]

31. Zhang, P.B.; Wei, M.L.; Li, Y.G.; Zhao, J.J.; Zheng, P.F.; Chen, J.M. Interactions of solute atoms with self-interstitial atoms/clusters in vanadium: A first-principles study. *J. Nucl. Mater.* **2021**, *553*, 153055. [CrossRef]
32. Iwakiri, H.; Wakimoto, H.; Watanabe, H.; Yoshida, N. Hardening behavior of molybdenum by low energy He and D ion irradiation. *J. Nucl. Mater.* **1998**, *258–263*, 873–878. [CrossRef]
33. Jiang, S.N.; Xu, L.Q.; Zheng, P.F. Evaluation of hardening behavior under synergistic interaction of He and subsequent H ions irradiation in vanadium alloys. *Nucl. Mater. Energy* **2018**, *16*, 19–23. [CrossRef]
34. Meyers, M.A. *Mechanical Behavior of Materials*; Cambridge University Press: Cambridge, UK, 2009; Chapter 4: Imperfections: Point and Line Defects.
35. Busby, J.T.; Hash, M.C.; Was, G.S. The relationship between hardness and yield stress in irradiated austenitic and ferritic steels. *J. Nucl. Mater.* **2005**, *336*, 267–278. [CrossRef]
36. Ribis, J.; Bordas, E.; Trocellier, P.; Serruys, Y.; Carlan, Y.; Legris, A. Radiation-sustained nanocluster metastability in oxide dispersion strengthened materials. *Nucl. Instrum. Methods Phys. Res. Sect. B Beam Interact. Mater. At.* **2015**, *365*, 22–25. [CrossRef]
37. Jung, H.J.; Edwards, D.J.; Kurtz, R.J.; Yamamoto, T.; Wu, Y.; Odette, G.R. Structural and chemical evolution in neutron irradiated and helium-injected ferritic ODS PM2000 alloy. *J. Nucl. Mater.* **2017**, *484*, 68–80. [CrossRef]
38. Sakasegawa, H.; Chaffron, L.; Legendre, F.; Boulanger, L.; Cozzika, T.; Brocq, M.; Carlan, Y. de Correlation between chemical composition and size of very small oxide particles in the MA957 ODS ferritic alloy. *J. Nucl. Mater.* **2009**, *384*, 115–118. [CrossRef]
39. Sakasegawa, H.; Legendre, L.; Boulanger, L.; Brocq, M.; Chaffron, L.; Cozzika, T.; Malaplate, J.; Henry, J.; Carlan, Y. de Stability of non-stoichiometric clusters in the MA957 ODS ferrtic alloy. *J. Nucl. Mater.* **2011**, *417*, 229–232. [CrossRef]
40. Swenson, M.J.; Wharry, J.P. The comparison of microstructure and nanocluster evolution in proton and neutron irradiated Fe-9% Cr ODS steel to 3 dpa at 500 C. *J. Nucl. Mater.* **2015**, *467*, 97–112. [CrossRef]
41. Slater, J.C. Atomic radii in crystals. *J. Chem. Phys.* **1964**, *41*, 3199–3204. [CrossRef]